Crustal and mantle structure beneath the southern Payenia Volcanic Province using gravity and magnetic data

A. Astort[1], B. Colavitto[1], L. Sagripanti[1], H. García[2], A. Echaurren[1], S. Soler[2], F. Ruíz[2], A. Folguera[1]

[1] Laboratorio de Geodinámica, IDEAN, Universidad de Buenos Aires, Conicet, Argentina.
[2] Instituto Geofísico Sismológico Ing. Volponi, Universidad Nacional de San Juan, Argentina.

Corresponding author: Astort Ana (anaastort@gl.fcen.uba.ar)

Key Points:

- A magmatic intrusion due to an asthenospheric upwelling in the Southern Central Andes was constrained by magnetic anomalies.
- The Geoid was used to interpret an asthenospheric upwelling.
- We found a correlation between drainage geometry, its diversion pattern and magnetic anomalies.

This article has been accepted for publication and undergone full peer review but has not been through the copyediting, typesetting, pagination and proofreading process which may lead to differences between this version and the Version of Record. Please cite this article as doi: 10.1029/2017TC004806

Abstract

The Auca Mahuida volcanic field lies on the southernmost Payenia Volcanic Province, one of the broadest retroarc volcanic plateaux in the southern Central Andes (~38° S). This voluminous basaltic flooding of Quaternary age was originated from a deep asthenospheric source, interpreted as a mantle plume product of changing slab dynamics. The geometry of this source is deduced from magnetotelluric data, but the limited spatial coverage of this array does not allow a detailed resolution of this anomaly. In order to present a detailed geometry of the conductive anomaly and related crustal magmatic bodies, we used multiple data sources. We combined Magnetic and Bouguer anomalies, Curie isotherm depth (T_c), Elastic Thickness (T_e) and Moho depth derived from the Global Earth Magnetic Anomaly Grid (EMAG2) and terrestrial gravity measurements, all together in a holistic geophysical analysis. The magnetic data depict a nearly 200 km-in-diameter circular anomaly that would correspond to a dense body according to the Bouguer anomaly. Geoid data from the Gravity Field Model (EIGEN-6c4) have been filtered in order to isolate deeper mass influences and visualize the asthenospheric upwelling previously described from magnetotelluric data. Moho inversion yields a crustal attenuation at 36-32 km depth coinciding with T_e below 20 km depth and a shallow T_c ($\leq$ 15 km depth) at the site where Geoid positive undulation was calculated. Finally, surface analysis allowed defining a topographic swell, compatible with the dimensions of the identified magnetic anomaly, where the main rivers deviated, potentially due to a recent base level change.

Introduction

The subduction of the Nazca plate beneath southwestern South America defines a partially continuous volcanic arc in the cordilleran axis, locally grouped as the South Volcanic Zone in the southern Central Andes (e.g., López-Escobar et al., 1977; Stern, 2004; Figure 1). From these latitudes and southward to Patagonia, genetically different Cenozoic volcanic units are scattered throughout the retroarc zone in Argentina, forming basaltic provinces associated with OIB-type within-plate magmatism (e.g., Rapela & Kay, 1988; Kay et al., 2005). As part of this latter group, south of the Chilean-Pampean flat-slab segment (~33º30'-38º S) and more than ~200 km away from the trench, the Payenia Volcanic Province develops (Figure 1). It corresponds to a less than ~ 2 Ma basaltic flooding, episodically erupted through hundreds of monogenetic cones and abundant lava flows, that encompasses more than ~40,000 km^2 and represents one of the broadest volcanic plateaux in the entire Andean mountain system (e.g., Folguera et al., 2009; Ramos & Folguera, 2011; Marchetti et al., 2014; Søager et al., 2015; Holm et al., 2016; Figure 1).

These volcanic rocks were emplaced over an attenuated lithosphere (Gilbert et al., 2006; Folguera et al., 2007; Søager et al., 2013; Spagnuolo et al., 2016), covering Neogene volcanic sequences with contrasting spatiotemporal and petrological characteristics (e.g., Folguera & Ramos, 2011). An eastward expansion of arc-like volcanism since ~17-5 Ma associated with a shallowing of the slab angle (e.g., Kay & Copeland, 2006; Kay et al., 2006 a,b; Ramos & Folguera, 2009), after which a within-plate geochemical signature of the younger products (< ~2 Ma) was recognized (Kay et al., 2006 a,b; Gudnason et al., 2012). Even more, within the volcanic province a southward decrease in the slab-derived fluids contribution to the parental magmas was observed (Ramos & Kay, 2006; Søager et al., 2013, 2015; May et al., 2018).

Sources associated with this anomalous retroarc magmatism were envisaged in the last years through considerable amounts of geophysical and geochemical data (Pesicek et al., 2012; Burd et al., 2014; Søager et al., 2013, 2015; Richarte et al., 2017), recognizing seismic and conductive anomalies corresponding to enriched mantle sources that fed the volcanic plateau. These were visualized as a complex plume head related to a slab tearing of the Nazca plate (Figure 1) (Pesicek et al., 2012; Gianni et al., 2017), branched into a series of smaller magmatic bodies impacting and storage beneath the southern Payenia Volcanic Province, such as the Auca Mahuida, Tromen, Los Volcanes and Payun Matru volcanic fields (Burd et al., 2014) (Figure 1).

Effects caused by a plume impact, such as the disruption of the thermal and density structure of the asthenosphere and lithosphere, voluminous volcanism and linkage with topographic swelling have widely been recognized in different geological settings (e.g., Cox, 1989; Parsons et al., 1994; Rainbird & Ernst, 2001; Saunders et al., 2005). However, no approach of this kind exists for the Payenia Volcanic Province, in particular, one of the broader Quaternary volcanic plateaux in the Andes. Besides, the presence of a slab tearing and complex plume geometry turns this setting into an exemplary study case for similar phenomena in other systems (Pesicek et al., 2012; Burd et al., 2013, 2104). Then, we want to study an asthenospheric anomaly related to a slab tearing in the Payenia Volcanic Province in the southern Central Andes, acquiring new high-resolution terrestrial gravity data and a compilation of magnetic anomalies (EMAG2) and gravity field (EIGEN-6C4) models. These datasets were used to calculate the reduced to the pole magnetic and Bouguer anomalies plus their respective residuals, derived maps of the gravimetric (inverted Moho and Elastic Thickness) and magnetic (Curie isotherm depth) data and Geoid filtering. Finally, the integration of this information with a geomorphological-morphometric analysis in the area constitutes a multidisciplinary approach with the aim of deciphering the causal relation of these processes.

2 Methodology and Datasets

To identify crustal anomalies in the Payenia Volcanic Province, we used magnetometric and terrestrial gravimetric data and the calculations of their derivate maps, such as the Moho depth, Elastic Thickness, and Curie isotherm depth. On the other hand, the deep structure was studied using Geoid data with the implementation of different filter techniques. Taking into account the different geodetic reference systems between the Geoid, terrestrial gravity, and magnetic data, we made a regional and qualitative common interpretation with caution.
Finally, we predict that the thermal anomaly may affect the topography, a hypothesis that is tested using drainage patterns analysis and swath profile techniques (methods details given below).

2.1 Magnetic Data

Magnetic anomalies constitute a powerful tool to obtain information about the subsurface when magnetic susceptibility contrasts are significant, as it is usually the case in sedimentary basins intruded by magmatic rocks. Magnetic data analyzed in this work correspond to the Global Earth Magnetic Anomaly Grid (EMAG2) compiled from satellite, ship and airborne magnetic measurements (*www.geomag.org/models/emag2.html*). The resolution of the grid is two arc minute (about 3.7 km) for a datum altitude of 4 km above the Geoid. The reduction process can be followed in Maus et al. (2009). A reduction to pole filter of MAGMAP FFT processing system was applied to the grid using IGRF data with 5.12º of declination and -37.7º of inclination. This filter addresses the problem of high amplitude corrections in low latitudes with an effective technique used in MAGMAP FFT processing system developed by

Grant and Dodds (1972) by using a second inclination to control the filter amplitude near the equator (Macleod et al., 1993). The 3-D analytic signal amplitude (ASA) was also computed following the expression of Roest et al. (1992). In the absence of remnant magnetic information due to the impossibility to access to deeply buried samples and at intermediate latitudes, the 3-D ASA enhances the interpretation (MacLeod et al., 1993; Rajagopalan, 2003) by comparing the ASA with the gravity and the RTP maps. Results were described in Section 3.1 and shown in Figure 3a,b,d, and e.

2.2 Gravity data

We calculated the Bouguer anomaly from terrestrial gravity data shown in Figure 2. These data correspond in part to the pre-existing gravimetric measurements database of the Instituto Geofísico-Sismológico Ing. Volponi (IGSV) (green points in Figure 2), while other points correspond to this work to complete and enhance the resolution of the Bouguer anomalies around the Auca Mahuida volcanic field (red points in Figure 2).

We corrected the data for the drift variations using the same reference point as the database. The Complete Bouguer Anomalies with the Free Air and Bouguer reductions were calculated following the classical expressions from Blakely (1996), with the observed gravity value tied to the IGSN 1971 system, and the normal gravity to the station latitude, taking the 1967 international ellipsoid. We took into account the Earth curvature and terrain correction according to the expression of LaFehr (1991) and Nagy (1966). Results are described in Section 3.1 and shown in Figure 3c and f. Throughout the results and figures, mGal unit was used (1 mGal = 10^{-5} m/s^2).

2.3 Spectrum Depth applied to magnetic and gravimetric anomalies

We calculated the radially averaged power spectrum *P* through the area of interest, using the Power Spectrum applied to the magnetometric and gravimetric data, with a window´s size of 200x200 km^2 as shown in Figure 3b. By the implementation of linear fits over the *Ln*(*P*) curve, it is possible to estimate the uppermost edge depth of the anomalous source using the relation $z=-s/4\pi$ between depth *z* and the linear fit slope *s* from Blakely (1996). To be able to compare gravimetric and magnetic spectral depths, 4 km were subtracted from magnetic depth results since the EMAG2 grid is presented originally at 4 km above the Geoid (Maus et al., 2009).

2.4 Inverted Moho

We calculated the five-dimensional inversion of the regional Bouguer anomaly prolonged 25 km upwards, using a five-layer model with densities increasing with depth, for determining the Moho topography (Figure 4a) (Introcaso, 1997; Arecco et al., 2015). We used for the crust a density of δ_c= 2650 kg/m^3, for the mantle δ_m= 3300 kg/m^3 and, for the transitional zone between the crust and mantle, three layers with increasing densities δ_1= 2700 kg/m^3, δ_2= 2800 kg/m^3 and δ_3= 2900 kg/m^3 every 10 km. Additionally, a correction to the Bouguer anomaly was made, using the gravimetric response of sediments with a density contrast of 300 kg/m^3, forming part of distinct depocenters of the Neuquén Basin that constitute the basement of the Payenia Volcanic Province, with a maximum thickness of 8 km (Sigismondi, 2012).

We considered Gardner's empirical velocity-density relation (Gardener et al., 1974; Brocher, 2005; Chullick et al., 2013) for the Neuquén Basin geological correction and crustal-mantle densities. Seismic velocities coming from the adjacent Atlantic passive margin were used since no vertical velocity models are available for the Neuquén Basin (Arreco et al., 2015). Results are described in Section 3.1 and shown in Figure 4a.

2.5 Effective Elastic Thickness

The flexural rigidity represents the lithospheric resistance to flexure under crustal and surficial loads. For long-term geological loads, the lithosphere is considered to respond regionally by flexure (Watts, 2001). Thermal heating is recognized as one of the causes for low values of effective elastic thickness and strength (Burov et al., 1995).

To calculate this parameter in the study area, we considered an elastic thin plate model of the lithosphere overlying a fluid substrate, with a flexural response $w(x, y)$ to the topographic load following the equations of Turcotte & Schubert (2002) and Watts (2001). We calculated a commonly used parameter equivalent to rigidity that is the Elastic Thickness (T_e) (results shown in Figure 4b), related both by the known expression that represents the vertical dimensions of a plate with Young module $E = 1.10^{11}$ *Pa* and a Poisson coefficient of $v = 0.25$ (Turcotte & Schubert, 2002).

Working in the wavenumber domain with module *k* (Watts, 2001), a Python code of forward modeling was implemented in order to calculate the effective Elastic Thickness T_e (Soler, 2015; García et al., 2016, 2017), where the basins are considered as buried loads using the term $\rho_t gh - ((\rho_{csup} - \rho_{sed})gh_{sed})$ instead of $\rho_t gh$, when it corresponds. The code requires two inputs: the topography and the Complete Bouguer Anomaly with the correction of the sedimentary effect for the Neuquén Basin area.

The method consists firstly in calculating the inverted gravimetric deflection W_{inv}, i. e. the inversion of the upper mantle-lower crust discontinuity (inverted gravity Moho). This discontinuity is obtained by the inversion of Bouguer anomalies over the whole study area (approximately 700x800 km^2) using the Parker-Oldenburg algorithm (Oldenburg, 1974) and adding a normal thickness of 35 km. The code contains an interface that allows the user to choose the size and position of the window, being T_e constant inside each window. We used window sizes between 70*x*70 km^2 and 200*x*200 km^2, which are optimum dimensions for local T_e analyses. No significant differences in $T_e$values were found using this range of windows size. A more detail description of the method and code can be found in García et al. (2017). For any particular chosen window several hypothetic values of T_e were considered and the respective deflection W_{local} was calculated. Each W_{local} was calculated considering the topographic load for the whole study area. All these W_{local} are later compared with the inverted gravimetric deflection inside the chosen window, and the most reliable T_e is the one that presents the minimum rms (root mean square). Sacek and Ussami (2009) have shown that the values of T_e from the forward modeling predict more effectively gravimetric anomalies in the foreland basin than the T_e values from spectral methods. The forward modeling code used in this work has the advantage of determining the deflection generated by the topographic load of the study area along the x-y plane, where each value of selected T_e represents a single and minimum rms. Finally, it is possible to choose a higher resolution window (70-200 km) looking for a better fit between the deflection of the elastic plate (which is calculated considering the influence of the entire topographic load of the area, even bigger than the interest area) and the inverted gravimetric deflection (García et al., 2017). Results are described in Section 3.1 and shown in Figure 4b.

2.6 Curie Isotherm Point

Applying the spectral analysis on the EMAG2 grid, the depth of the Curie Isotherm can be approximated (Figure 4c) using the Tanaka et al. (1999) method. It is worth noting that the Curie temperature depends on the mineralogy of the magnetic bodies, so the Curie surface cannot be directly interpreted as an isothermal surface. The intensity of the magnetization depends on the existing magnetic mineralogical phases and on the volume fraction of them in the crust. However, Frost and Shive (1986) demonstrated that for the lower crust, the magnetite in an almost pure state constitutes the most important source of magnetism, being there 570°C the Curie point. For this purpose, we computed the map of magnetic anomalies considering windows of $dx = dy$ =50 km.

Considering the magnetized surface of the crust as a horizontal plate with infinite lateral extension, the base (Curie Isotherm depth), top and centroid, Z_b, Z_t and Z_c of this plate can be calculated (Tanaka et al., 1999; Ruiz & Introcaso, 2004), where the three depths are related through the linear expression $Z_b = 2Z_c - Z_t$. The Z_t and Z_c can be calculated from a linear fit over the Radial Average Power Spectrum following the logarithmic expressions for long and short wavelengths from Tanaka et al. (1999). The altitude datum of EMAG2 was subtracted from the resulting Curie isotherm depth in order to be referenced to the Geoid. Results are described in Section 3.1 and shown in Figure 4c.

2.7 Geoid

The Geoid data used on this work correspond to the Gravity Field Model EIGEN-6C4 (Förste et al., 2014) from the calculation service website ICGEM database at GFZ Potsdam (*http://icgem.gfz-potsdam.de*). This model approximates the Gravitational Potential using an Expansion of Spherical Harmonics up to degree and order 2190 and fitted with satellite and terrestrial data. The EIGEN-6C4 includes data from LAGEOS, GRACE, GOCE, surface data DTU Global gravity anomalies, DTU Ocean Geoid and EGM2008 Geoid grid (Förste et al., 2014).

2.7.1 Geoid spectral analysis

For rather simple studies there is a relationship between the spectral composition of the Geoid and the depth of the anomalous mass that induces a particular wavelength, $Z_n = \frac{R_{earth}}{(n-1)}$, where n refers to the degree of the expansion, Z_n to the maximum depth for the density mass causing the Geoid anomaly and R_{earth} is the earth radius, (Bowin, 1983). Even though an inherent non-uniqueness feature of the geopotential must be considered when this relationship is applied, the visualization of depth layers of the Geoid results in a convenient tool (results shown in Figures 5 and 6).

Thus, Geoid residuals (R_n) were obtained by subtracting different truncated expansions of the Geoid (N_n) to the full Geoid expansion (N_{total}), i.e., $R_n=N_{total}-N_n$ in order to emphasize the shallower anomalous sources and to filter the deeper source components such as the core-mantle boundary and deep mantle transitions.

Although this filter methodology is not really rigorous, it allows visualization of the shallower components as a first approximation. To constrain the interpretation, a 3-D density model (Tassara et al., 2006 and Tassara and Echaurren, 2012) was used with the purpose of calculating the subducting Nazca plate and topography contributions to the Geoid over the study area. The 3-D density model was performed by the authors using the IGMAS modeling software (Interactive Gravity and Magnetic Application System; Götze, 1984, 2014; Götze & Lahmeyer, 1988; Götze et al., 2017; Schmidt & Götze, 1998; Schmidt et al., 2011; Breunig et al., 2000; Alvers et al., 2014, 2015). The model densities and geometry were taken from the

original model of Tassara et al. (2006), with the only exception of the geometry of the Nazca plate at the latitudinal range of 37.5-39°S, where the tearing and a horizontal detachment described by Pesicek at al. (2012) were added affecting the slab below 200 km depth. Additionally, the topography reliefs with a density of 2670 kg/m^3 were added to the 3-D density model using the ETOPO1 Global Relief Model to calculate the topography contribution.

The modified-subducting Nazca plate contribution was calculated using a mean density super plus of 20 kg/m^3 following the methodology used in Götze and Kirchner (1997). Results are described in Section 3.2 (Figures 5, 6 and 7).

2.8 Surface analysis

Several studies have demonstrated the sensitivity of the fluvial network to active tectonics, isostatic readjustments and deep mantle dynamics (Pazzaglia et al., 1998; Keller et al., 1999; Wobus et al., 2006; Kirby & Whipple, 2012; Molin et al., 2012, among others). With the aim to analyze potential topographic changes due to mantle flow dynamics and magmatic emplacement, we performed a regional geomorphological map focused on drainage patterns and river terraces. We accompanied this analysis developing longitudinal stream and swath profiles. Geomorphological regional mapping was accomplished using ArcGIS software and SRTM (30 m) DEM data to observe small changes in altitude related to fluvial scarps and terraces particularly focused in the main fluvial courses, the Colorado and Neuquén rivers (Figures 1). Swath and longitudinal stream profiles were extracted from the SRTM (30 m) DEM using TopoToolbox, a set of functions for topographic analysis implemented in Matlab programming language (Schwanghart & Kuhn, 2010; Schwanghart & Scherler, 2014). We performed four 200 km-long swath profiles crossing the area of interest with an NE-trending orientation and a regular width of 20 km. These swath profiles condense maximum, mean and minimum elevation data to a single topographic chosen profile allowing a broader visualization of the topographic variations and a more accurate visualization of the relief. To study the stream profiles, we used the power law function which relates the channel slope with the drainage area (Wobus et al., 2006; Kirby & Whipple, 2012). Changes in concavity and knickpoints were studied in order to identify possible topographic anomalies that could correlate with regions of potential ongoing topographic uplift. In this analysis, we assume a steady-state river incision into bedrock (Hack, 1973; Whipple & Tucker, 1999; Whipple, 2004). See the results described in Section 3.3 (Figures 8 and 9).

3 Results

3.1 Gravimetric and magnetic derived maps

The total magnetic intensity (Figure 3a) exhibits a dipolar shape with the magnetization direction expected for the normal polarity in the Southern hemisphere. The reduced to pole (RTP) anomaly (Figure 3b) shows a high contrast of susceptibility beneath and to the southeast of the Auca Mahuida volcanic field. The RTP anomaly, with values at around 100 nT, depicts a circular area (actually in a closer look it rather corresponds to a horseshoe shape) with ~200 km in diameter. Two principal magnetic highs can be recognized through the circular magnetic anomaly (CMA), one located at the northeast, named northeast magnetic anomaly high (NEH), and a second at the southwest, named southwest magnetic anomaly high (SWH) (Figure 8).

The CMA spatially matches the 33, 52 and 129 km depth contours of the 35 Ohm-m low resistivity isosurface of Burd et al. (2014). This isosurface has been identified by these authors as a conductive structure and interpreted as a plume impacting the lower crust,

steeply dipping to the east up to ~400 km depth. On the other hand, the CMA coincides with a relatively high-density region with a value of -50 mGal contrasting with the surroundings that, according to the Bouguer Anomaly (Figure 3c), has an average value of -100 mGal.

The Analytic Signal Amplitude (ASA) calculated from the total magnetic field (Figure 3d) presents maxima marking the edges of magnetized bodies that partially coincide with the CMA highs (southwest highs -SWH- and northeast highs -NEH-). The Figure (3e) corresponds to a residual of the magnetic anomaly calculated from an upward prolongation of 15 km and with a reduction to the pole. Even though the filtering of the CMA long wavelength was not possible due to its significant intensity and amplitude, the residual reveals the presence of a shallower, north-oriented magnetic linear feature below the western sector of the Auca Mahuida volcanic field. This shallower magnetic feature is spatially associated with a high-density anomaly in the residual of the Bouguer data (Figure 3f) and to the marked edges presented in the ASA map. The magnetic bodies depicted by the ASA coincide with shallow anomalies present in the gravity residual (Figure 3f), while the RTP anomaly probably represents both shallow and deep components.

From the gravimetric data spectrum, the slope of the first linear fit yields an approximate depth of 27 km, which most likely coincides with the Moho discontinuity. However, it is worth noting that this should be taken as a general approximation since such a comparison is done between a field that has not been prolonged (gravity spectrum depths) and a field upwardly continued up to 25 km (Moho calculation).

The slope of the third linear fit would be the interface sediment-basement at approximately 6.4 km depth. Finally, the slope of the intermediate linear fit, from the gravimetric data spectrum, evidences a depth of 17.57 km that most likely indicates the top of a high-density body which coincides with the CMA magnetic anomaly identified at the mid-crust. On the other hand, from the spectral analysis performed over magnetic data, two trends are discerned: while one seems to reflect the Curie isotherm depth at 22.22 km, the second most likely represents the interface between the sediment infill and the basement at 8.18 km depth.

In a more regional analysis, the inverted Moho computed from the Bouguer anomaly (Figure 4a) presents deeper values of less than 40 km depth along the highest topographic zone to the west of the Payenia Volcanic Province, while to the east these values become shallower reaching ~32-28 km depth (vertical empty rectangle as a reference in Figure 4).

Elastic Thickness (Figure 4b) shows a trend of low values between 10-20 km depth in coincidence with the Payenia Volcanic Province and the CMA area (68-70°W) and another trend of low values between 66 and 67°W that coincides with a shallower Moho (see complete calculated T_e map in the Supporting Information; Figure S1).

Finally, an approximate Curie isotherm depth map (Figure 4c), computed from the magnetic data (EMAG2), presents a north-oriented anomaly at 66-67°W, with values that go from 14 to 18 km depth. To the west, deeper values from 22 to 32 km depth coincide with the areal extent of the Neuquén Basin. The CMA is placed at the edge of the Neuquén Basin in the transition zone between shallower and deeper values of the calculated Curie isotherm. These shallower Curie isotherm values match the inverted Moho (~32 km in depth), and the low resistivity area determined from previous MT survey by Burd et al. (2014), interpreted by these authors as an asthenospheric upwelling (see Supporting Information for the MT results from Burd et al. 2014, Figure S2).

3.2 Geoid and filtered Geoid

The full expansion of the Geoid, N_{total}, shown in Figure 5a, is produced by the influence of shallow and deep masses. Figure 5b corresponds to the residual Geoid $R_{30} = N_{total} - N_{30}$ that represents the sum of the different components from 220 km depth up to the Earth surface, evidencing a negative undulation elongated between 64-68°W with ~300-400 km in width through longitude. Figure 5c corresponds to the residual $R_{60} = N_{total} - N_{60}$ that reflects the different components from 100 km depth up to the Earth surface. In this residual, a smooth positive undulation appears, partially hiding the previous negative undulation, separated from the area of maximum topography in the high Andes to the west. This positive undulation becomes more evident in $R_{90} = N_{total} - N_{90}$ (Figure 5d) that reflects mass influences between 70 km depth and the surface. Since the negative undulation described in R_{30} (Figure 5b) starts to vanish in R_{60} (Figure 5c), the causative masses are inferred to be placed approximately between the 220 and 100 km depth beneath the Earth surface.

Figure (6) shows a 3-D perspective constructed with residuals of the Geoid series at different degrees that imply different source depths. Towards the east of the CMA, the negative undulation is evidenced at 220 km depth and remains up to 160 km depth.

We observe the main source (positive undulation) between 70 and 35 km depth to the east of the southern Payenia Volcanic Province that ramifies into smaller sources, one beneath the Auca Mahuida volcanic field (Figure 6).

Figure 7a shows a cross-section at 38ºS selected from a 3-D density model modified from Tassara et al. (2006) that includes the tearing of the subducted Nazca plate at 37.5-39°S, determined from seismic data (Pesicek et al., 2012) (see Supporting Information for the seismic results from Pesicek et al. 2012, used to constrain the model; Figure S3). The Moho calculated from the gravity data (Figure 4a) was used to control the crust-mantle boundary of the model, although no significant differences were found between the original and the modified model. After including the slab modified geometry, the calculated gravity fits regionally the Bouguer anomaly (taken from the Eigen6-c4 model), where the red dashed line indicates the calculated gravity with the IGMAS forward modeling software, and the solid red line is the Bouguer anomaly from Eigen6-c4 model (Figure 7a). The subducted slab contribution to the Geoid (purple dashed line) is superposed to the Eigen6-c4 full-expansion of the Geoid (solid black line). The contribution does not exceed the maximum of the Geoid, decreasing to a minimum of 10 m below the Geoid towards the east. Figure 7b presents the same profiles at 38ºS superposed to the topography contribution (green dashed line) and the result of subtracting the subducted Nazca plate and topography contributions to the full expansion of the Geoid (blue dashed line). The topography contribution increases in the maximum relief area up to 23 m, not exciding the maximum for the full expansion of the Geoid. The pink solid line corresponds to the Residual R60 from the Figure 5c. The black box coincides with the areas indicated in Figures 4, 5 and 6, where low Elastic values, shallower Curie and shallower Moho coincide with a subtle positive undulation.

3.3 Surface analysis

Fluvial patterns of the Colorado and Neuquén rivers, over the CMA (Figure 8), reveal some distinctive characteristics, where deviations of both main courses resemble this magnetic anomaly. First, near 68°W, the Colorado River shows a nearly southward orthogonal deviation, producing a rotation of the channel section coincidently with the northeast magnetic anomaly high (NEH). Based on our reconstructions, the Colorado River would have had an initial E-directed flow that gradually would have changed to SE, S and finally SW directed (Figure 8). This process has left out four paleo-channels with a particular fan-shape

arrangement (described previously by Niviere et al. 2013), in which consecutive channels (5-2; Figures 8 and 9c) exhibit a progressive lower altitude. Fan shape morphology, river deviation and successive deepening of channels are interpreted as being associated with successive changes in base level, presumably related to an uplift produced through the NEH. Similarly, the Neuquén River shows a deviation of its course to the south in coincidence with the southwest magnetic anomaly high (SWH) of the CMA. Fluvial terraces and a paleo-channel to the north of the present river course may be indicating that in the past the Neuquén River flowed in an NNW direction (Figure 8).

Morphometric analysis of the Neuquén and Colorado rivers were conducted obtaining two stream longitudinal profiles (Figure 9 a, b), which show a general concave up shape. Locations of observed knickpoints (black dots in Figure 8) show a strong correlation with the edges of the CMA magnetic anomaly. In particular, the Colorado River presents three knickpoints, one 200 km out of the study area, corresponding to a lithological contrast (knickpoint-1). However, knickpoint-2 is placed over the SWH, suggesting a relation with base level changes, although lithological contrasts produced by a basaltic flow cannot be totally discarded. Finally, the easternmost knickpoint-3, in the Colorado River, is located over the zone where the paleo-channels migrated to the south, indicating a change in the base level producing a modification in the drainage. The Neuquén River presents two knickpoints, one of which is located at the edge of the SWH (knickpoint-4) (Figure 8).

Finally, four swath profiles built across the CMA anomaly show a good correlation with a regional swell topographic feature (profiles 2, 3, 4 in Figure 8). This swell reaches 500-700 m in height in coincidence with the maximum values of the CMA magnetic anomaly, implying that the topography could be at a certain extent controlled by magmatic injection at depth (Figure 8).

4 Discussion and conclusions

The determined CMA magnetic anomaly, of nearly 200 km in diameter, correlates with the shallower low resistivity isosurfaces from Burd et al. (2014) (at 33, 52 and 129 km depth) (see Figure 3b), and is slightly displaced to the west (~100 km) respect to the determined Geoid positive undulations, shallower Moho and shallower Curie isotherm depths (Figures 4 and 6).

From the spectrum depth analysis, the top of the magnetic body causing the CMA would be placed in the mid-crust, approximately at 17.57 km depth from the surface land, possibly extending even deeper as a function of its exact shape, since the method only detects its shallower part. Additionally, this body could extend locally to the upper crust based on the residuals and ASA anomalies that are interpreted as the presence of shallower magmatic bodies (Figure 3d, e, and f). From the Bouguer anomaly and its residual, it is evident that the CMA coincides with high gravity values indicating higher densities than the host rocks, which could be interpreted as mafic and cold materials intruding the middle to upper crust (Figures 3c and 3f).

Curie isotherm depth, Moho geometry, and Elastic Thickness display N-elongated anomalies at 66-67°W to the east of the Payenia Volcanic Province. In particular, the Curie isotherm depth throughout this area presents shallower values with respect to the surroundings between 18 and 15 km depth, consistent with an upwardly deflected thermal density structure. Besides, the Moho is at shallower 36-32 km depths in contrast with values up to 40 km depth to the west, on the Andean foothills. Finally, the Elastic Thickness exhibits low values (10-35 km in the study area) that abruptly rise up to 80 km toward the east in the foreland zone, where the Curie isotherm depth gets deeper and where the Río de La Plata craton is placed.

Geoid analysis allows describing an asthenospheric anomaly that matches with previous MT anomaly interpreted as a mantle plume beneath the Payenia Volcanic Province. Geoid residuals reveal a negative undulation (negative density contrast) with a source at least as deep as 220 km depth, changing to a positive undulation (positive density contrast) in shallower levels (Figures 5c, d, and 6). The density contrast at deeper levels is interpreted as a consequence of partially molten materials with less density than the surrounding asthenospheric mantle, while the shallower contrast evidences an excess in density that could be due to the upward deflection of the density-mantle structure and the presence of high-density materials emplaced above the 100 km depth. Therefore, an upward deflection of the asthenospheric structure seems to be evidenced by the Geoid residuals, in accordance with a shallower Curie isotherm and a shallower Moho (Figure 10). These are coherent with the models initially proposed by Burd et al. (2014), in which a mantle plume is impacting the base of the continental lithosphere with a slight westward deflection imposed by mantle drag forces associated with the trench-retreat of the subducted Nazca plate.

When subtracting the geoidal effects of the Nazca plate and topography from the full expansion of the Geoid, a subtle positive undulation still remains, in coincidence with the area of mantle upwelling determined in magnetotelluric data (Burd et al., 2014). 3-D density modeling produced by IGMAS, modifying pre-existing models from recently released seismic tomography data, shows that topography and ocean slab contributions consist of long wavelengths with maximums on the highest relief area to the west of the described anomaly developed over the foreland area, precluding a connection between them.

The 200 km-in-diameter circular magnetic anomaly coinciding with high gravity values is interpreted as a laccolith-like magmatic body intruding the mid-crust, feeding the southern Payenia Volcanic Province at the Auca Mahuida volcanic field. Strong deflections of main rivers flowing across the foreland zone and valley abandonment could be explained by a broad regional swelling seen in morphometric analyses, potentially due to magmatic injection associated with asthenospheric upwelling and subducted Nazca plate-tearing at depth.

Acknowledgments

We acknowledge revisions made by two anonymous Reviewers and Associate and Principal Editor that allowed improving this work. This work was financed by "Evolución tectónica de los Andes entre los 39° y los 45°S. Determinación temporal y espacial de las distintas etapas contraccionales y de las potenciales reactivaciones extensionales en los Andes Nordpatagónicos. Director: Andrés Folguera y Vanesa Litvak. **PIP 2015-2017.**

We acknowledge the use of the IGMAS modeling software (Interactive Gravity and Magnetic Application System) for the 3-D density model calculations. Particular thanks are given to Sabine Schmidt for personal support regarding the use of this software.

Magnetic (EMAG2) and Gravity Field Model data (EIGEN-6c4) used in this study are available at the public repository at www.geomag.arg/models/emag2.html and icgem.gfz-potsdam.de. The images were generated by Generic Mapping Tools (GMT).

This is the R------ contribution of the Instituto de Estudios Andinos Don Pablo Groeber, University of Buenos Aires, Conicet.

References

Alvers, M. R., Barrio-Alvers, L., Bodor, C., Gotze, H. J., Lahrneyer, B., Plonka, C., & Schmidt, S. (2015). ¿Quo vadis inversión?. *First break*, 33(4), 65-74.

Alvers, M. R., Götze, H. J., Barrio-Alvers, L., Schmidt, S., Lahmeyer, B., & Plonka, C. (2014). A novel warped-space concept for interactive 3D-geometry-inversion to improve seismic imaging. *First Break*, 32(4).

Arecco, M. A., Ruiz, F., Pizarro, G., Giménez, M., Martínez, P., & Ramos, V. A. (2015). Gravimetric determination of the continental–oceanic boundary of the Argentine continental margin (from 36° S to 50° S). *Geophysical Journal International*, *204*(1), 366-385.

Blakely, R. J. (1996). *Potential theory in gravity and magnetic applications*. Cambridge University Press.

Bowin, C. (1983). Depth of principal mass anomalies contributing to the earth's geoidal undulations and gravity anomalies∗. *Marine Geodesy*, *7*(1-4), 61-100.

Breunig, M., Cremers, A. B., Götze, H. J., Schmidt, S., Seidemann, R., Shumilov, S., & Siehl, A. (2000).
Geological mapping based on 3D models using an Interoperable GIS. *GIS-HEIDELBERG-*, 13(2),12-18.

Brocher, T. M. (2005). Empirical relations between elastic wavespeeds and density in the Earth's crust. *Bulletin of the seismological Society of America*, *95*(6), 2081-2092.

Burd, A. I., Booker, J. R., Mackie, R., Pomposiello, C., & Favetto, A. (2013). Electrical conductivity of the Pampean shallow subduction region of Argentina near 33°S: evidence for a slab window. *Geochemistry, Geophysics, Geosystems*, *14*(8), 3192-3209.

Burd, A. I., Booker, J. R., Mackie, R., Favetto, A., & Pomposiello, M. C. (2014). Three-dimensional electrical conductivity in the mantle beneath the Payún Matrú Volcanic Field in the Andean backarc of Argentina near 36.5°S: Evidence for decapitation of a mantle plume by resurgent upper mantle shear during slab steepening. *Geophysical Journal International*, *198*(2), 812-827.

Burov, E. B., & Diament, M. (1995). The effective elastic thickness (T e) of continental lithosphere: what does it really mean?. *Journal of Geophysical Research: Solid Earth*, 100(B3), 3905-3927.

Chulick, G.S., Detweiler, S., & Mooney, W.D., (2013). Seismic structure of the crust and uppermost mantle of south america and surrounding oceanic basins. *Journal of South American Earth Sciences* 42, 260–276

Cox, K. G. (1989). The role of mantle plumes in the development of continental drainage patterns. *Nature*, *342(6252)*, 873.

Folguera, A., Introcaso, A., Giménez, M., Ruiz, F., Martinez, P., Tunstall, C., ... & Ramos, V. A. (2007). Crustal attenuation in the Southern Andean retroarc (38–39° 30′ S) determined from tectonic and gravimetric studies: the Lonco-Luán asthenospheric anomaly. *Tectonophysics*, *439*(1), 129-147.

Folguera, A., Naranjo, J. A., Orihashi, Y., Sumino, H., Nagao, K., Polanco, E., & Ramos, V. A. (2009). Retroarc volcanism in the northern San Rafael Block (34–35° 30′ S), southern Central Andes: Occurrence, age, and tectonic setting. *Journal of Volcanology and geothermal Research*, *186*(3), 169-185.

Folguera, A., & Ramos, V. A. (2011). Repeated eastward shifts of arc magmatism in the Southern Andes: a revision to the long-term pattern of Andean uplift and magmatism. *Journal of South American Earth Sciences*, *32*(4), 531-546.

Förste, C., Bruinsma, S., Abrikosov, O., Flechtner, F., Marty, J. C., Lemoine, J. M., ... & Biancale, R. (2014*). EIGEN-6C4-The latest combined global gravity field model including GOCE data up to degree and order 1949 of GFZ Potsdam and GRGS Toulouse*. In EGU General Assembly Conference Abstracts (16).

Frost, B. R., & Shive, P. N. (1986). Magnetic mineralogy of the lower continental crust. *Journal of Geophysical Research: Solid Earth*, *91*(B6), 6513-6521.

García, García, H., Soler, S., Gianni, G.M., Ruiz, F., (2016). Análisis flexural de la cuenca Cretácico-Paleógena del noroeste Argentino. *La subcuenca Lomas de Olmedo: zona de transición entre dos mecanismos de deformación distintivos.* In: Primer Simposio de Tectónica Sudamericana. Chile.

García, H. P., Gianni, G. M., Lupari, M. N., Sánchez, M. A., Soler, S. R., Ruiz, F., & Klinger, F. G. L. (2017). Effective elastic thickness in the Central Andes. Correlation to orogenic deformation styles and lower crust high-gravity anomaly. *Journal of South American Earth Sciences.*

Gardner, G. H. F., Gardner, L. W., & Gregory, A. R. (1974). Formation velocity and density—The diagnostic basics for stratigraphic traps. *Geophysics*, *39*(6), 770-780.

Gianni, G. M., García, H. P., Lupari, M., Pesce, A., & Folguera, A. (2017). Plume overriding triggers shallow subduction and orogeny in the southern Central Andes. *Gondwana Research*, 49, 387-395.

Gilbert, H., Beck, S., & Zandt, G. (2006). Lithospheric and upper mantle structure of central Chile and Argentina. *Geophysical Journal International*, *165*(1), 383-398.

Götze, H. J. (1984). *Über den Einsatz interaktiver Computergraphik im Rahmen 3-dimensionaler Interpretationstechniken in Gravimetrie und Magnetik* (Doctoral dissertation, Technische Universität Clausthal).

Götze, H. J., & Lahmeyer, B. (1988). Application of three-dimensional interactive modeling in gravity
and magnetics. *Geophysics*, 53(8), 1096-1108.

Götze, H. J., & Kirchner, A. (1997). Gravity field at the South American active margin (20 to 29°S). *Journal of South American Earth Sciences*, 10(2), 179-189.

Götze, H. J. (2014). Potential methods and geoinformation systems. *Handbook of Geomathematics*, 1-21.

Götze, H. J., Schmidt, S., & Menzel, P. (2017). Integrative Interpretation of Potential Field Data by 3D-Modeling and Visualization. *Oil Gas European Magazine*, *43*(4), 202-208.

Grant, F. S., & Dodds, J. (1972). MAGMAP FFT processing system development notes: Paterson Grant and Watson Ltd.

Gudnason, J., Holm, P. M., Søager, N., & Llambías, E. J. (2012). Geochronology of the late Pliocene to recent volcanic activity in the Payenia back-arc volcanic province, Mendoza Argentina. *Journal of South American Earth Sciences*, 37, 191-201.

Hack, J. T. (1973). Stream-profile analysis and stream-gradient index. *Journal of Research of the US Geological Survey*, *1*(4), 421-429.

Holm, P. M., Søager, N., Alfastsen, M., & Bertotto, G. W. (2016). Subduction zone mantle enrichment by fluids and Zr–Hf-depleted crustal melts as indicated by backarc basalts of the Southern Volcanic Zone, Argentina. *Lithos*, *262*, 135-152.

Introcaso, A. (1997), *Gravimetría*, Rosario, UNR Editora.

Kay, S. M., Godoy, E., & Kurtz, A. (2005). Episodic arc migration, crustal thickening, subduction erosion, and magmatism in the south-central Andes. *Geological Society of America Bulletin*, *117*(1-2), 67-88.

Kay, S. M., & Copeland, P. (2006). Early to middle Miocene backarc magmas of the Neuquén Basin: Geochemical consequences of slab shallowing and the westward drift of South America. *Geological Society of America Special Papers*, 407, 185-213.

Kay, S. M., Mancilla, O., & Copeland, P. (2006a). Evolution of the late Miocene Chachahuén volcanic complex at 37° S over a transient shallow subduction zone under the Neuquén Andes. *Geological Society of America Special Papers*, 407, 215-246.

Kay, S. M., Burns, W. M., Copeland, P., & Mancilla, O. (2006b). Upper Cretaceous to Holocene magmatism and evidence for transient Miocene shallowing of the Andean subduction zone under the northern Neuquén Basin. *Geological Society of America Special Papers*, 407, 19-60.

Keller, E. A., Gurrola, L., & Tierney, T. E. (1999). Geomorphic criteria to determine direction of lateral propagation of reverse faulting and folding. *Geology*, *27*(6), 515-518.

Kirby, E., & Whipple, K. X. (2012). Expression of active tectonics in erosional landscapes. *Journal of Structural Geology*, 44, 54-75.

LaFehr, T. R. (1991). An exact solution for the gravity curvature (Bullard B) correction. *Geophysics*, *56*(8), 1179-1184.

Lopez-Escobar, L., Frey, F. A., & Vergara, M. (1977). Andesites and high-alumina basalts from the central-south Chile High Andes: geochemical evidence bearing on their petrogenesis. *Contributions to Mineralogy and Petrology*, *63*(3), 199-228.

MacLeod, I. N., Jones, K., & Dai, T. F. (1993). 3-D analytic signal in the interpretation of total magnetic field data at low magnetic latitudes. *Exploration Geophysics*, 24(3/4), 679-688.

Marchetti, D. W., Hynek, S. A., & Cerling, T. E. (2014). Cosmogenic 3 He-exposure ages of basalt flows in the northwestern Payún Matru volcanic field, Mendoza Province, Argentina. *Quaternary Geochronology*, 19, 67-75.

Maus, S., Barckhausen, U., Berkenbosch, H., Bournas, N., Brozena, J., Childers, V., ... & Gaina, C. (2009). EMAG2: A 2–arc min resolution Earth Magnetic Anomaly Grid compiled from satellite, airborne, and marine magnetic measurements. *Geochemistry, Geophysics, Geosystems*, *11*(8).

May, V., Chivas, A., Dosseto, A., Honda, M., Matchan, E., Phillips, D. & Price, D. (2018). Quaternary volcanic evolution in the continental back-arc of southern Mendoza, Argentina. *Journal of South American Earth Sciences, 84 (2018), 88-103.*

Molin, P., Fubelli, G., Nocentini, M., Sperini, S., Ignat, P., Grecu, F., & Dramis, F. (2012). Interaction of mantle dynamics, crustal tectonics, and surface processes in the topography of the Romanian Carpathians: a geomorphological approach. *Global and planetary change*, *90*, 58-72.

Nagy, D. (1966). The gravitational attraction of a right rectangular prism. *Geophysics*, *31*(2), 362-371.

Nivière, B., Messager, G., Carretier, S., & Lacan, P. (2013). Geomorphic expression of the southern Central Andes forebulge (37° S, Argentina). *Terra Nova*, *25*(5), 361-367.

Oldenburg, D. W. (1974). The inversion and interpretation of gravity anomalies. *Geophysics*, *39*(4), 526-536.

Parsons, T., Thompson, G. A., & Sleep, N. H. (1994). Mantle plume influence on the Neogene uplift and extension of the US western Cordillera?. *Geology*, *22*(1), 83-86

Pazzaglia, F. J., Gardner, T. W., & Merritts, D. J. (1998). Bedrock fluvial incision and longitudinal profile development over geologic time scales determined by fluvial terraces. *Rivers over rock: fluvial processes in bedrock channels*, 207-235.

Pesicek, J. D., Engdahl, E. R., Thurber, C. H., DeShon, H. R., & Lange, D. (2012). Mantle subducting slab structure in the region of the 2010 M 8.8 Maule earthquake (30–40° S), Chile. *Geophysical Journal International*, *191*(1), 317-324.

Rainbird, R. H., & Ernst, R. E. (2001). The sedimentary record of mantle-plume uplift. *Special Papers-Geological Society of America*, 227-246.

Rajagopalan, S. (2003). Analytic signal vs. reduction to pole: solutions for low magnetic latitudes. *Exploration Geophysics*, *34*(4), 257-262.

Ramos, V. A., & Kay, S. M. (2006). Overview of the tectonic evolution of the southern Central Andes of Mendoza and Neuquén (35–39° S latitude). *Geological Society of America Special Papers*, *407*, 1-17.

Ramos, V. A., & Folguera, A. (2009). Andean flat-slab subduction through time. *Geological Society, London, Special Publications*, *327*(1), 31-54.

Ramos, V. A., & Folguera, A. (2011). Payenia volcanic province in the Southern Andes: An appraisal of an exceptional Quaternary tectonic setting. *Journal of Volcanology and geothermal Research*, *201*(1), 53-64.

Rapela, C. W., & Kay, S. M. (1988). Late Paleozoic to Recent magmatic evolution of northern Patagonia. *Episodes*, *11*(3), 175-182.

Richarte, D., Lupari, M., Pesce, A., Nacif, S., & Gimenez, M. (2018). 3-D crustal-scale gravity model of the San Rafael Block and Payenia volcanic province in Mendoza, Argentina. *Geoscience Frontiers*, *9*(1), 239-248.

Roest, W. R., Verhoef, J., & Pilkington, M. (1992). Magnetic interpretation using the 3-D analytic signal. *Geophysics*, *57*(1), 116-125.

Ruiz, F., & Introcaso, A. (2004). Curie point depths beneath Precordillera Cuyana and Sierras Pampeanas obtained from spectral analysis of magnetic anomalies. *Gondwana Research*, *7*(4), 1133-1142.

Sacek, V., & Ussami, N. (2009). Reappraisal of the effective elastic thickness for the sub-Andes using 3-D finite element flexural modelling, gravity and geological constraints. *Geophysical Journal International*, *179*(2), 778-786.

Saunders, A. D., England, R. W., Reichow, M. K., & White, R. V. (2005). A mantle plume origin for the Siberian traps: uplift and extension in the West Siberian Basin, Russia. *Lithos*, *79*(3-4), 407-424.

Schmidt, S., & Götze, H. J. (1998). Interactive visualization and modification of 3D-models using GIS- functions. *Physics and Chemistry of the Earth*, 23(3), 289-295.

Schmidt, S., Plonka, C., Götze, H. J., & Lahmeyer, B. (2011). Hybrid modelling of gravity, gravity gradients and magnetic fields. *Geophysical Prospecting*, *59*(6), 1046-1051.

Schwanghart, W., & Kuhn, N. J. (2010). TopoToolbox: A set of Matlab functions for topographic analysis. *Environmental Modelling & Software*, *25*(6), 770-781.

Schwanghart, W., & Scherler, D. (2014). TopoToolbox 2-MATLAB-based software for topographic analysis and modeling in Earth surface sciences. *Earth Surface Dynamics*, *2*(1), 1.

Sigismondi, M. E. (2012). *Estudio de la deformación litosférica de la cuenca Neuquina: estructura termal, datos de gravedad y sísmica de reflexión* (Doctoral dissertation, Ph. D. Thesis, Universidad de Buenos Aires, Buenos Aires, 1-367).

Søager, N., Holm, P. M., & Llambías, E. J. (2013). Payenia volcanic province, southern Mendoza, Argentina: OIB mantle upwelling in a backarc environment. *Chemical Geology*, *349*, 36-53.

Søager, N., Portnyagin, M., Hoernle, K., Holm, P. M., Hauff, F., & Garbe-Schönberg, D. (2015). Olivine major and trace element compositions in southern Payenia basalts, Argentina: evidence for pyroxenite–peridotite melt mixing in a back-arc setting. *Journal of Petrology*, *56*(8), 1495-1518.

Soler, S. R. (2015). *Métodos Espectrales para la Determinación de la Profundidad del Punto de Curie y el Espesor Elástico de la Corteza Terrestre.* Master's thesis, Facultad de Ciencias Exactas, Ingeniería y Agrimensura Universidad Nacional de Rosario.

Spagnuolo, M. G., Orts, D. L., Gimenez, M., Folguera, A., & Ramos, V. A. (2016). Payenia Quaternary flood basalts (southern Mendoza, Argentina): Geophysical constraints on their volume. *Geoscience Frontiers*, *7*(5), 775-782.

Stern, C. R. (2004). Active Andean volcanism: its geologic and tectonic setting. *Revista geológica de Chile*, *31*(2), 161-206.

Tanaka, A., Okubo, Y., & Matsubayashi, O. (1999). Curie point depth based on spectrum analysis of the magnetic anomaly data in East and Southeast Asia. *Tectonophysics*, *306*(3), 461-470.

Tassara, A., Götze, H. J., Schmidt, S., & Hackney, R. (2006). Three-dimensional density model of the Nazca plate and the Andean continental margin. *Journal of Geophysical Research: Solid Earth*, *111*(B9).

Tassara, A., & Echaurren, A. (2012). Anatomy of the Andean subduction zone: three-dimensional density model upgraded and compared against global-scale models. *Geophysical Journal International*, *189*(1), 161-168.

Turcotte, D. L., & Schubert, G. (2002). *Geodynamics*, 456 pp. Cambridge Univ. Press, New York.

Watts, A. B. (2001). *Isostasy and Flexure of the Lithosphere*. Cambridge University Press.

Whipple, K. X. (2004). Bedrock rivers and the geomorphology of active orogens. *Annu. Rev. Earth Planet. Sci.*, *32*, 151-185.

Whipple, K. X., & Tucker, G. E. (1999). Dynamics of the stream-power river incision model: Implications for height limits of mountain ranges, landscape response timescales, and research needs. *Journal of Geophysical Research: Solid Earth*, *104*(B8), 17661-17674.

Wobus, C., Whipple, K. X., Kirby, E., Snyder, N., Johnson, J., Spyropolou, K., ... & Sheehan, D. (2006). Tectonics from topography: Procedures, promise, and pitfalls. *Geological Society of America Special Papers*, *398*, 55-74.

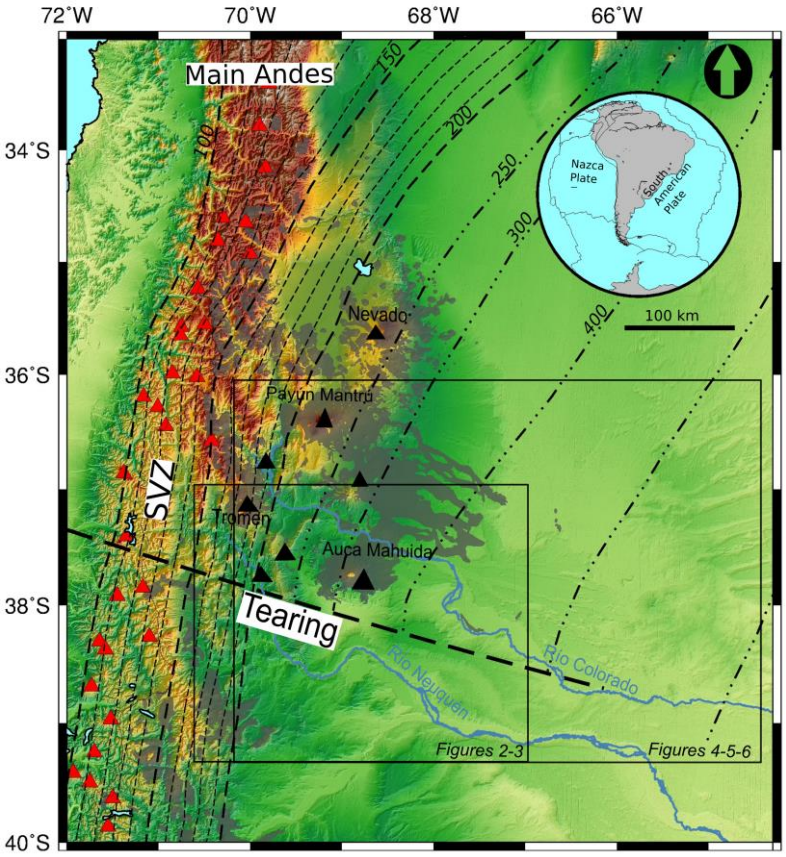

Figure 1: *Digital elevation model (SRTM-NASA) showing younger than 2 My basalts (dark grey shades) from the Payenia Volcanic Province of the retroarc of the southern Central Andes (modified from Kay et al., 2006b; Kay & Copeland, 2006; Ramos & Folguera, 2009, 2011). Projection of the tearing found on the Nazca plate at depth from seismic tomographies is shown as a thick dashed line (Pesicek et al., 2012). Iso-depth contours of the Nazca plate in kilometers are shown in thin dashed lines (data from Burd et al. 2013 and 2014, and references therein). Red and black triangles represent less than 2 My volcanic centers of the South Volcanic Zone (SVZ in red color) and the Payenia Volcanic Province (in black), respectively.*

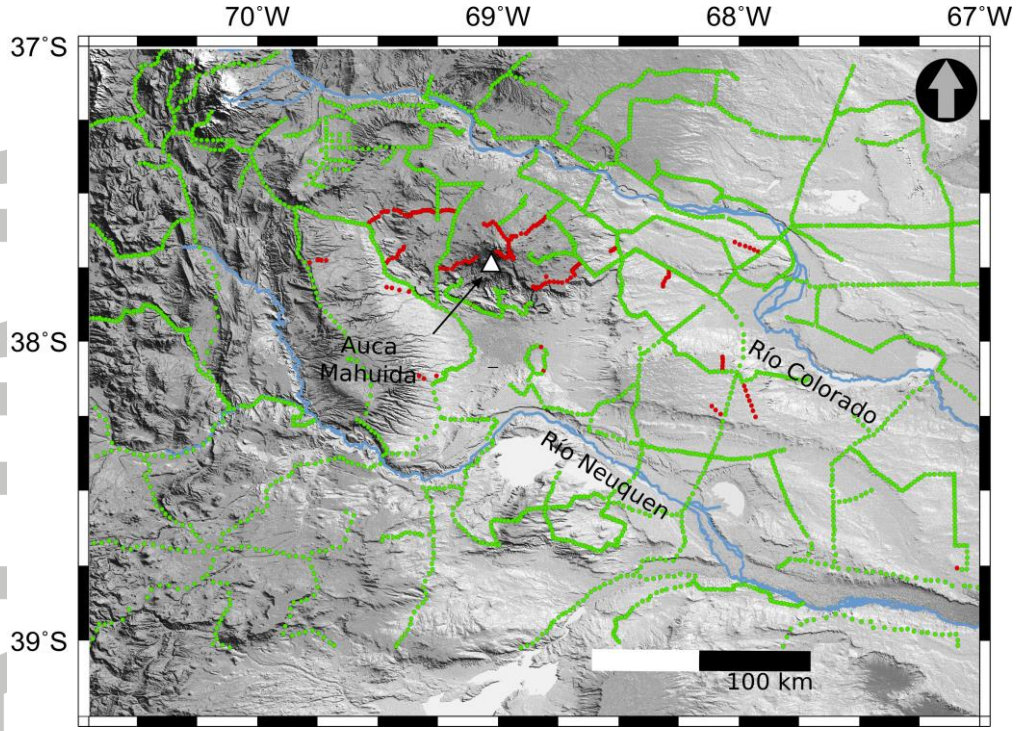

Figure 2: *Digital elevation model (grey shades) superimposed by the positions of gravity stations which were used in this study. Green points indicate points of the IGSV database (Instituto Geofísico Sismológico Ing. Volponi), and red ones are the new measurements. Refer to Fig. 1 for a regional perspective. The white triangle corresponds to the summit part of the Auca Mahuida volcanic field.*

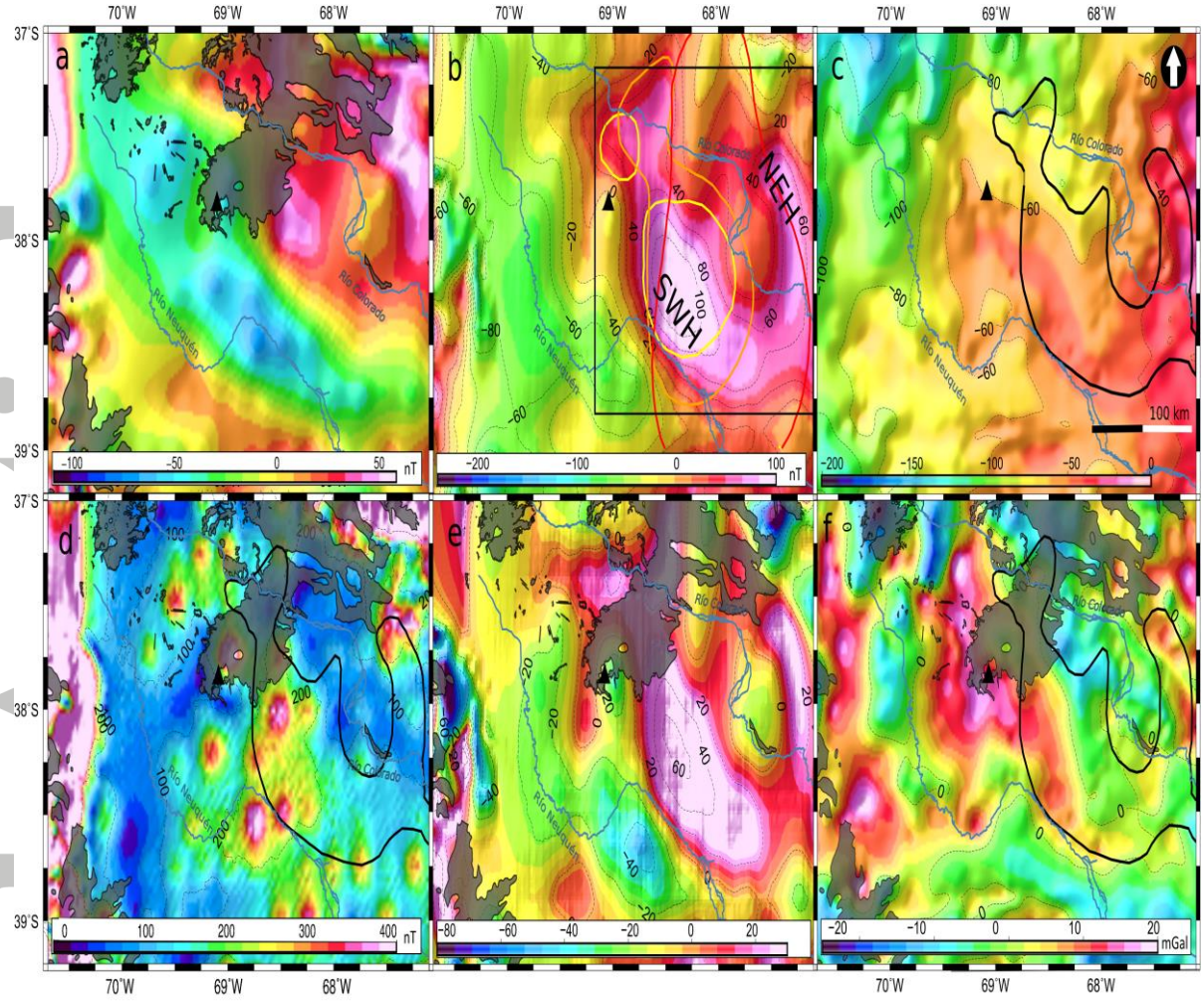

Figure 3: *Magnetic and gravimetric anomalies and their relation to volcanism in the southern Payenia Volcanic Province. a) Total magnetic intensity exhibits a dipolar shape. b) Reduced to pole magnetic anomaly (nT) that delineates the circular magnetic anomaly (CMA) nearly 200 km in diameter. This anomaly is interpreted as caused by mafic rocks intruded in the mid-crust with a higher density than surrounding rocks. The color curves represent the resistivity isosurface of 35 Ohm-m from Burd et al. (2014) (yellow, orange, and red lines correspond to 33, 52 and 129 km depth, respectively) showing in map-view the spatial correlation with the CMA located in the crust. The black box represents the windows size for spectral analysis used to calculate the radially averaged power spectrum to identify the anomaly depth. c) Bouguer anomaly (given in mGal). High gravity values overlay the area of CMA. The -60 mGal contour line corresponds with the edge of the CMA. d) The analytic signal amplitude of the total magnetic intensity highlights edges that partially coincide with the CMA. e) Residual of magnetic anomaly discounting a 15 km upward prolongation with a Reduced to Pole filter applied. Basaltic lava flows of less than 2 My are drawn in grey as a reference. f) Residual field of Bouguer anomaly at a height of 25 km prolonged upwards (it is superposed with the CMA and basalts field). Colorado and Neuquén rivers draining the retroarc through both the area of CMA and basaltic outcrops. See Figure 1 for location in a regional perspective. The two principal magnetic highs are indicated in b), the Northeast magnetic anomaly high (NEH), and the Southwest magnetic anomaly high (SWH).*

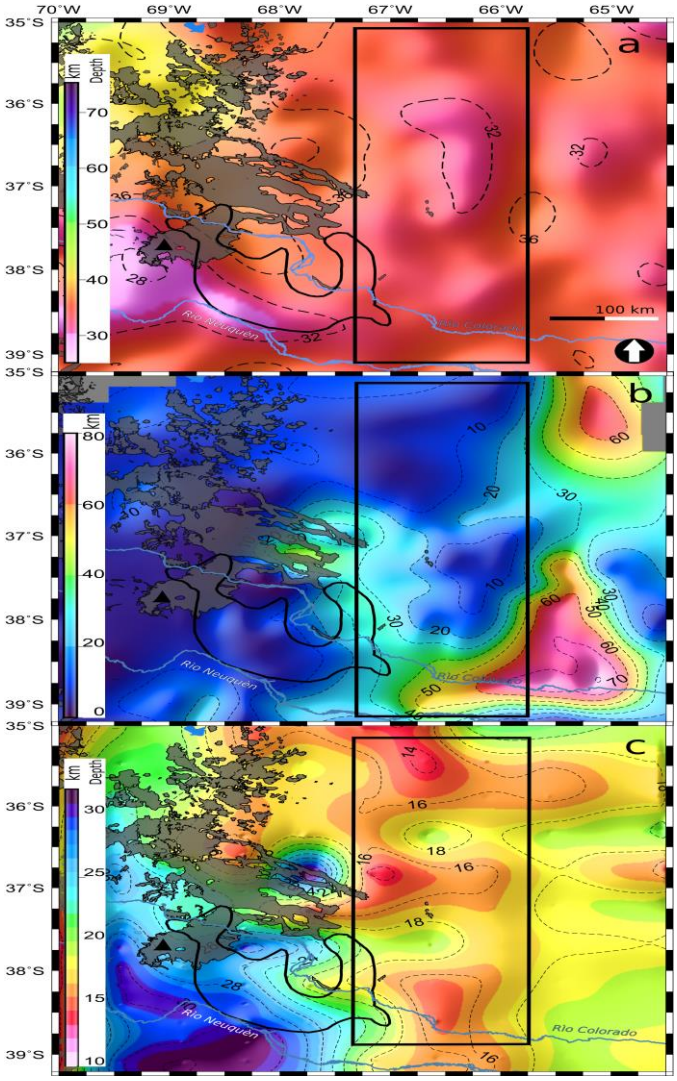

Figure 4: *Thermal and flexural state of the southern Payenia Volcanic Province and their relation to Moho topography. a) Inverted Moho depth map (contour lines indicate depth in km), where shallower depths are between 66 and 67ºW. The dark grey area indicates the approximate circular shape (horseshoe geometry) of the depicted magnetic anomaly (CMA). The light grey area corresponds to younger than 2 Ma retroarc volcanism of the Payenia Volcanic Province. b) Elastic thickness map with contour lines that indicate thickness in km. c) Curie isotherm map with contour lines that indicate the estimated depth of the 570º C isotherm in km. Note that the Curie isotherm is shallower to the east of the Payenia Volcanic Province reaching ~15 km depth, through a North-oriented stripe around 66-67ºW. Vertical rectangle to the east of the Payenia Volcanic Province indicates the approximate position of the (a) stretched crust (shallower Moho), (b) relatively lower (T_e), and (c) shallower Curie isotherm (T_c). See Figure 1 for location in a regional perspective.*

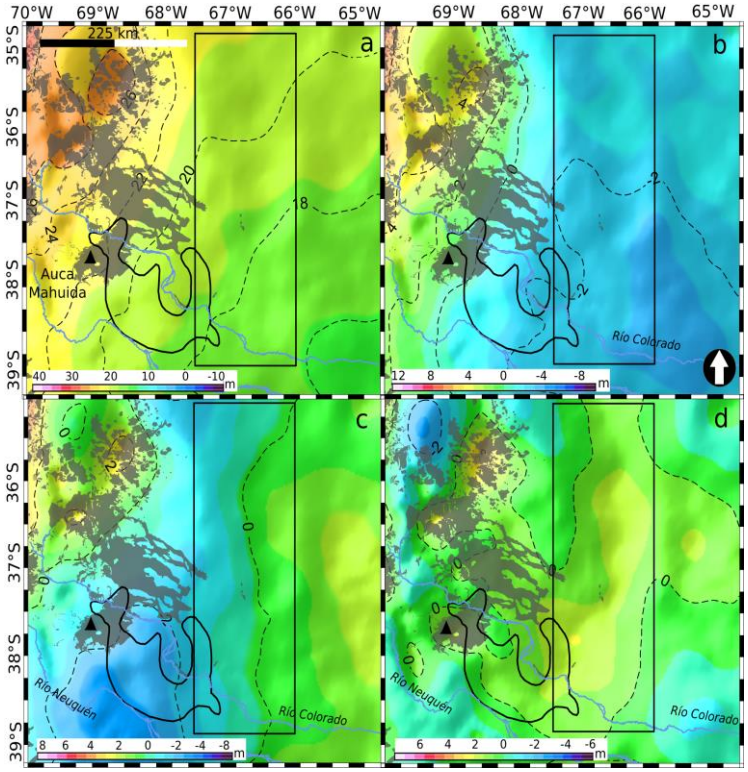

Figure 5*: Full and truncated Geoid expansions in the Payenia Volcanic Province. a) Full expansion of Geoid: Geoid undulation [m] superposed to the Payenia Volcanic Province and the CMA anomaly as a reference in grey. b), c) and d) calculated Geoid residuals in order to analyze the different depths components in depth, at 220, 100, and 70 km respectively. Note that the Geoid residuals depict, between 70-100 km depths, positive undulations to the east of the area of retroarc volcanic eruptions. Rectangle coincides with the area indicated in Figure 4 that depicts shallower values of Curie isotherm, thinner Elastic Thicknesses and shallower Moho interface.*

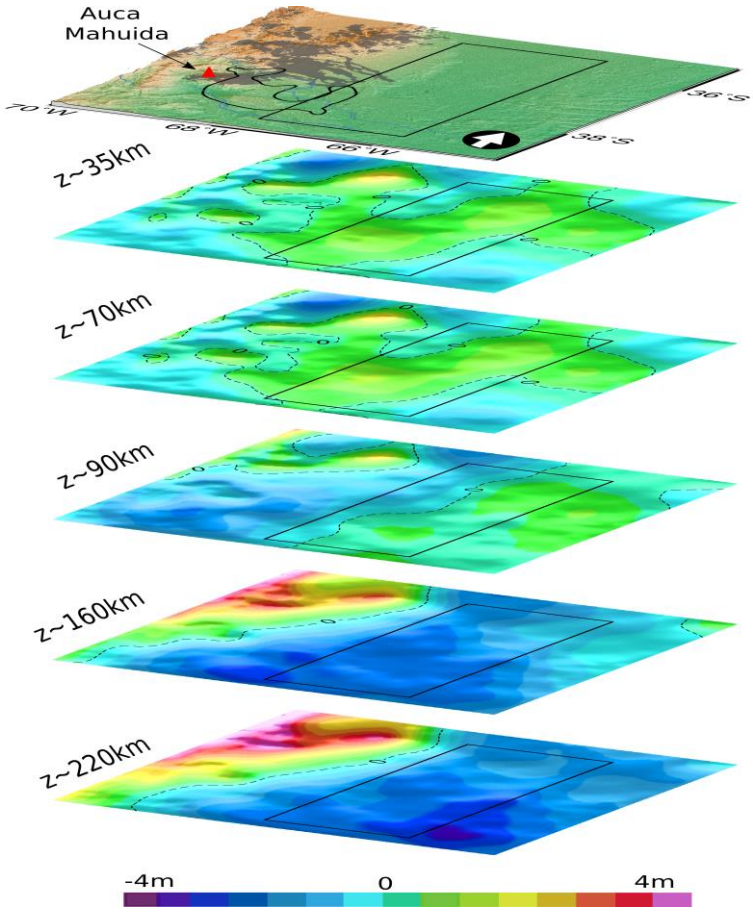

Figure 6: *Residuals of truncated Geoid at different depths. Note the main source (positive undulation) between 70 and 35 km depth to the east of the southern Payenia Volcanic Province. The empty rectangle area encloses the area with shallower values of the Curie isotherm, Moho depth, and thinner Elastic Thickness (see Figure 4). Note a general correlation between the Geoid positive undulation and these parameters. The southern Payenia Volcanic Province, the Auca Mahuida volcanic field, and the CMA (see Figures 1 and 3) are shown as references.*

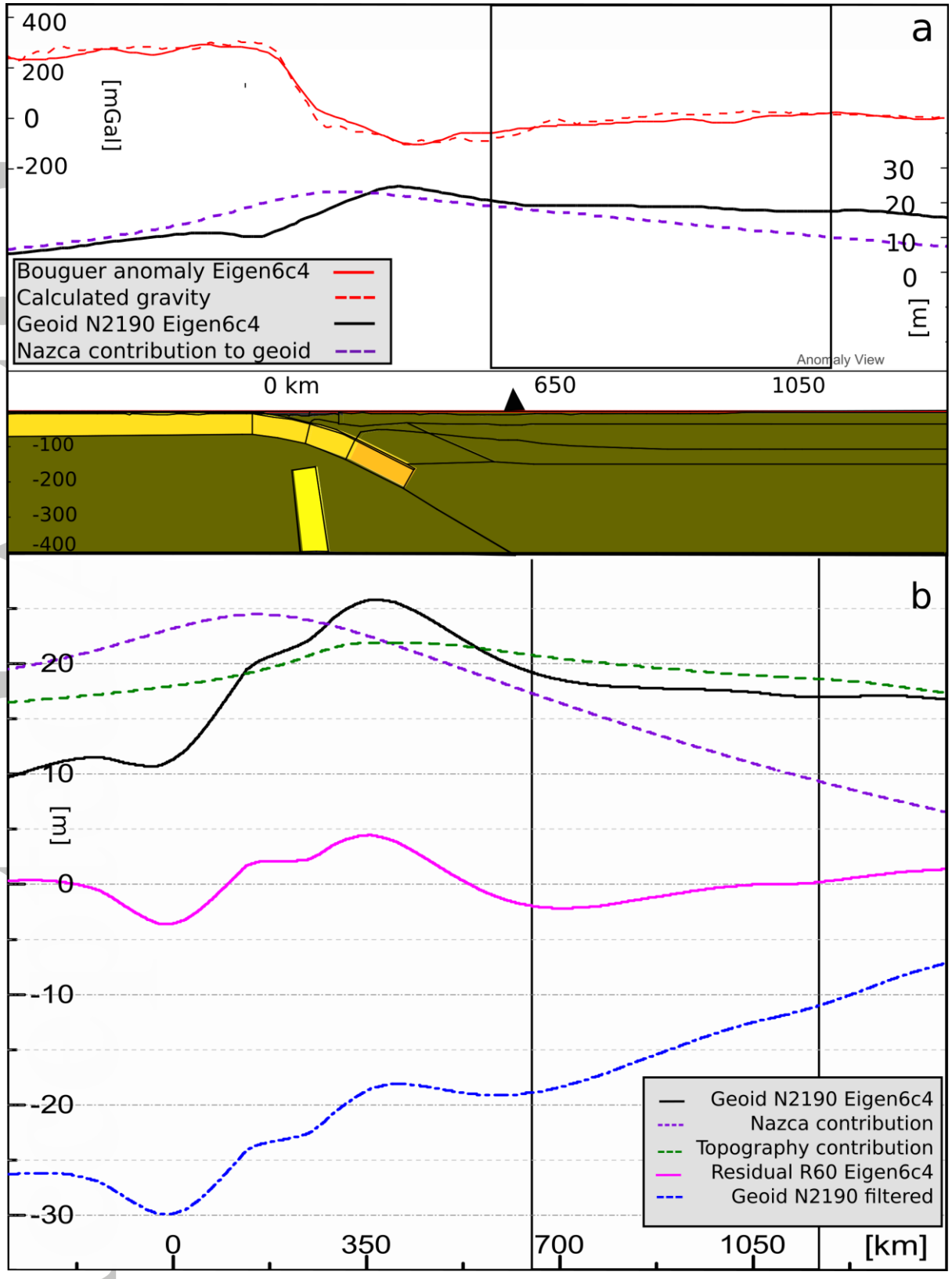

Figure 7: *The subducted Nazca plate and topography contributions to the Geoid. a) One of the cross sections (38ºS) of the modified 3-D model from Tassara et al. (2006) calculated with IGMAS software, after including the tearing of the Nazca plate (yellow) and the*

horizontal detachment interpreted in Pesicek et al. (2012). Because of the vertical tearing, the Nazca plate penetrates into the mantle a depth lower than 200 km (Pesicek et al., 2012). A vertical slab is stagnant, between 200-400 km depth, as a consequence of the horizontal detachment (Pesicek et al., 2012). The Nazca plate contribution (purple dash line) to the Geoid was calculated considering a mean density super plus of 20 kg/m^3. The black solid line corresponds to the full-expansion of the model Eigen6-c4 in figures a) and b). The model fits regionally the Bouguer gravity anomaly (dashed and solid red line). b) Profiles at 38ºS: Full expansion of the Eigen6c4 Geoid model (solid black line); topography (green dashed line) and subducted slab (purple dashed line) contributions to the calculated Geoid. The residual R60 from the Figure 5c (pink solid line) and finally the filtered Geoid without the contributions of the subducted Nazca plate and the topography are shown (blue dashed line). The black box in a) and b) coincides with the area indicated in Figures 4, 5 and 6, where low Elastic thickness values, shallower Curie isotherm and shallower Moho coincide with a subtle positive undulation.

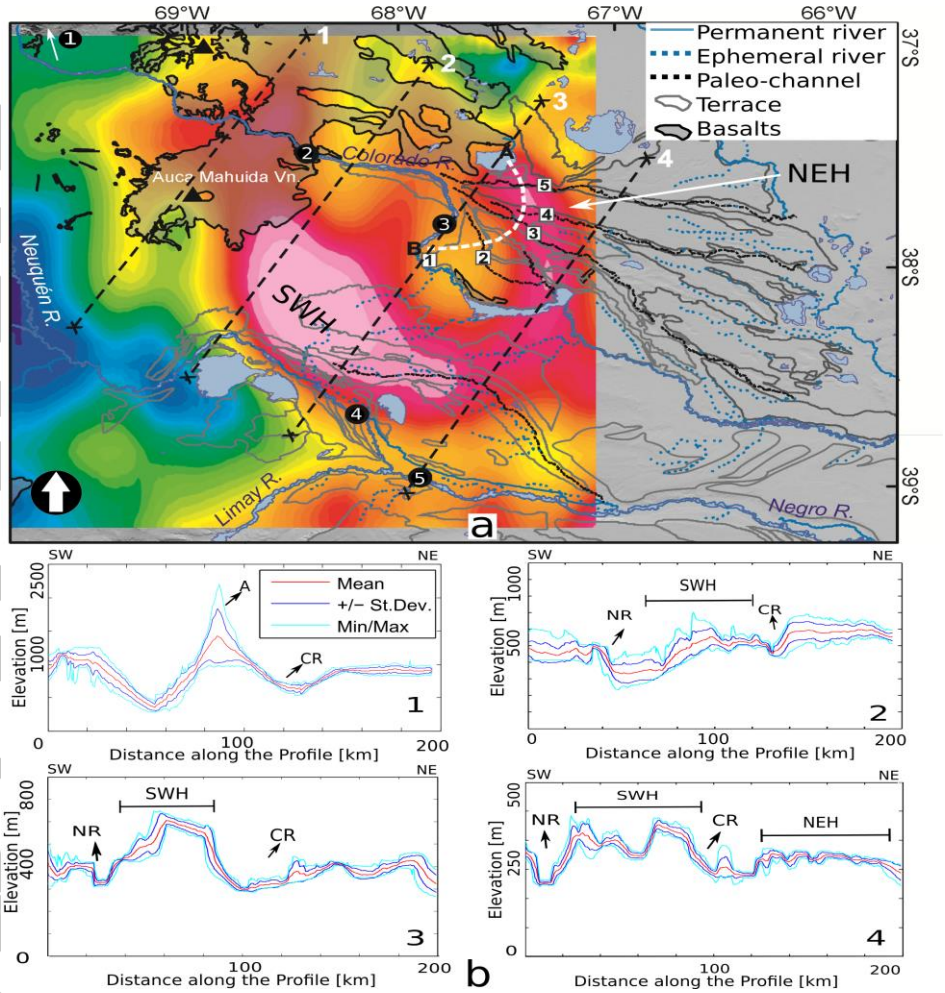

Figure 8: *Fluvial drainage and swath profiles of the Colorado and Neuquen rivers.* a) *Digital elevation model in grey (SRTM 90 m) showing the fluvial drainage and main fluvial landforms from the Colorado and Neuquén rivers over a hypothetically domed structure affecting the foreland zone coincident with the CMA. The numbers in the black dots correspond to knickpoints identified in the equilibrium profiles in Figure 9. A fan-shape arrangement with paleo-channels (where the white dashed line indicates proposed lateral wandering of the Colorado River, while resulting paleo-channels are numbered 5-2 with corresponding numbers indicated in white boxes) is described for the catchment of the Colorado River. b) Below, the location of swath profile curves (numbered 1 to 4 with lengths of 200 km each) are indicated with dashed black lines in the map above. The main features of the swath profiles are indicated as A: Auca Mahuida volcanic field, CR: Colorado River, NR: Neuquén River, SWH: Southwest high elevation and NEH: Northeastern high elevation. Note that the SWH and NEH match the areas of maximum magnetic values.*

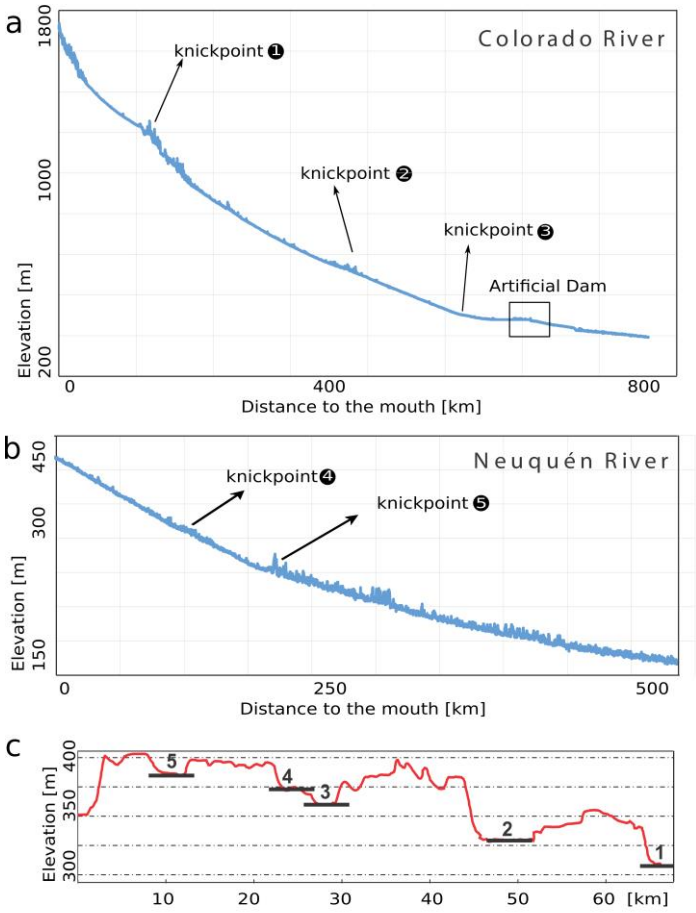

Figure 9: *Stream profiles of the Colorado and Neuquén rivers and interpreted paleo-channels of the Colorado River. a) and b) The knickpoints in the stream profiles curves could indicate a non-state of equilibrium of the rivers flowing across the foreland zone in coincidence with the migration segments indicated in Figure 8. The westernmost knickpoint 1 is out of the study area, approximately 300 km away and most likely corresponds to a lithological contrast associated with an incision in a basalt plateau at 36°15'S, 69°38'W. The black box in (a) indicates the position of an artificial dam that most likely affects locally the natural course of the Colorado River. c) Topographic profile corresponding to the white dashed line in Figure 8 over the paleo-channels of the Colorado River that exhibits a decrease in altitude for the terraces migrating from the location 5 to 1 on the diagram.*

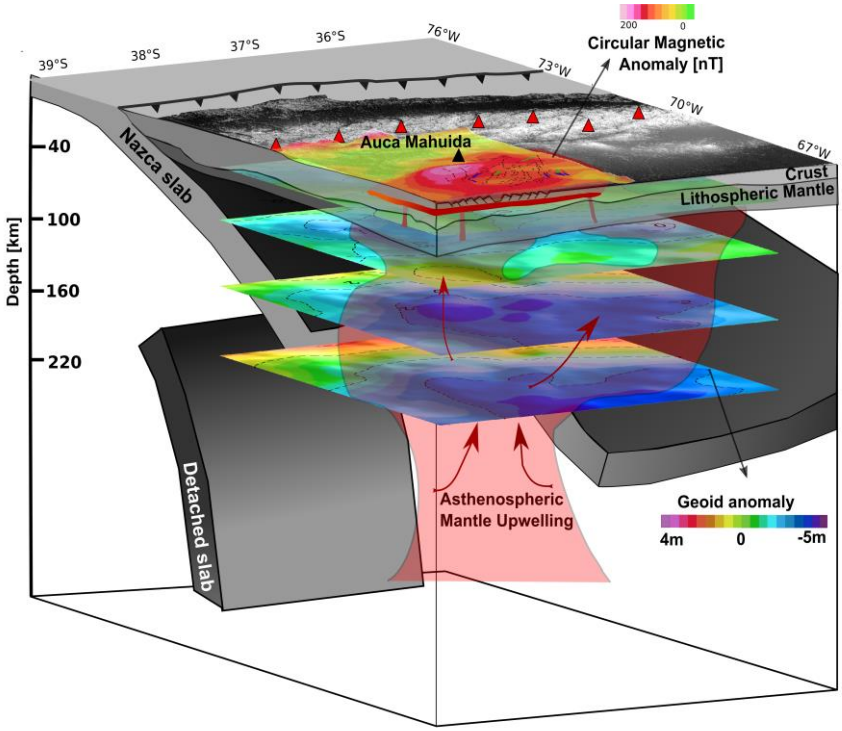

Figure 10: *Schematic model of the southern Payenia Volcanic Province and underlying crust and mantle that shows a general correlation between the slab tearing interpretation from seismic tomography data (Pesicek et al., 2012), and plume geometry interpreted from MT data (Burd et al., 2014) and from EMAG2 and our gravimetric data. The reduced to pole magnetic anomaly map is projected over the topography that allows interpreting a mafic body intruding the mid-crust. This magmatic body would be fed from an asthenospheric mantle upwelling that is reconstructed from the Geoid anomaly slices shown in Figure 6. The interface crust-lithospheric mantle shows attenuated values in coincidence with the area of inferred asthenospheric upwelling.*